

Emission of OAM entangled photon pairs in a nonlinear ring fiber utilizing spontaneous parametric down-conversion

D. Javůrek*

*RCPTM, Joint Laboratory of Optics of Palacký University and Institute of Physics of AS CR,
17. listopadu 12, 771 46 Olomouc, Czech Republic*

J. Svozilík

*RCPTM, Joint Laboratory of Optics of Palacký University and Institute of Physics of AS CR,
17. listopadu 12, 771 46 Olomouc, Czech Republic and
ICFO-Institut de Ciències Fotòniques, Mediterranean Technology Park,
Av. Carl Friedrich Gauss 3, 08860 Castelldefels, Barcelona, Spain*

J. Peřina Jr.

*Institute of Physics, Joint Laboratory of Optics of Palacký University and Institute of Physics of AS CR,
17. listopadu 50a, 771 46 Olomouc, Czech Republic*

We suggest the generation of photon pairs in a thermally induced nonlinear periodically-poled silica fiber by spontaneous parametric down-conversion. Photons are generated directly in eigenstates of optical angular momentum. Photons in a pair can be entangled in these states as well as in frequencies. We identify suitable spatial and polarization modes giving an efficient nonlinear interaction. By changing the pump field properties both narrow- and broad-band down-converted fields can be obtained.

PACS numbers: 42.65.Lm,42.81.Qb,42.50.Ex

I. INTRODUCTION

Entangled photon fields represent a corner-stone for various experimental implementations of quantum systems due to their highly nonclassical behavior. Entanglement of photons is crucial in many applications including quantum computing [1, 2], quantum metrology [3, 4] and quantum object identification [5]. It is important also in the area of quantum random walks where it brings new dimension into the problem [6, 7]. Entanglement is indispensable also for quantum communication protocols that, among others, include quantum teleportation [8] and secured quantum key distribution networks [9, 10]. Systems for wavelength-division-multiplexing that allow to distribute polarization entangled photons among multiple users [11, 12] serve as typical examples.

In the above described applications, entangled photon pairs generated in a nonlinear medium with non-zero $\chi^{(2)}$ susceptibility via the process of spontaneous parametric down-conversion (SPDC) [13–15] serve as typical resources. The entangled fields called signal and idler emerge instantly after the annihilation of a pump photon. The nonlinear process encompassing the pump, signal and idler photons satisfies the conservation law of energy and phase-matching (PM) conditions [16]. Whereas the conservation law of energy originates in homogeneity of time and is automatically fulfilled, the phase-matching conditions for wave vectors cannot be satisfied in a typical material with normal dispersion. However, this prob-

lem can be overcome by utilizing birefringent materials or periodical poling of nonlinear materials [17–19]. Also, the modal PM found in waveguides allows to compensate additionally the naturally occurring phase mismatch [20]. Alternatively, wide possibilities for achieving PM are offered by nonlinear photonic structures [21, 22].

The problem of phase matching occurs also in the considered nonlinear thermally poled silica fibers in which their material dispersion is modified by their geometry (waveguiding dispersion). Fortunately, the process of periodical poling of $\chi^{(2)}$ susceptibility [23–25] for these fibers has been mastered. It allows to achieve phase matching of the nonlinearly interacting fields, together with the conservation law of energy. During the poling, a SiO₂ material with no natural $\chi^{(2)}$ susceptibility (due to symmetry) is heated up and exposed to a strong electric field originating in the electrodes inserted in the fiber. The free ions in the fiber are dragged by the field and form the macroscopic charge nearby the electrodes. When the material is cooled down back to the room temperature, the electric field is switched off. However, the ions remain frozen at their positions and form a permanent internal static electric field [25, 26]. This field is responsible for nonlinear properties of SiO₂. The nonlinear grating is created by a UV erasure process that removes the nonlinearity inside domains exposed to a UV laser. The created nonlinear grating provides an additional momentum to phase matching conditions of the nonlinear interaction. Suitable choice of this momentum then allows to reach quasi-phase-matching (QPM) of the overall nonlinear process.

In the considered optical fiber, we concentrate our attention to guided modes with a defined mode of orbital

*Electronic address: javurek@slo.upol.cz

angular momentum (OAM) [27–30]. Such modes have been theoretically studied [29, 30] and experimentally characterized recently [29] using a ring or vortex geometry (concentric rings) of optical fibers. This geometry allows to separate modes of the LP₁₁ family that differ in their effective refractive indices. This results in their stable propagation with a low ratio of crosstalk for lengths over 1 km. Such stable states of OAM can then be exploited to multiplex data and rise the transfer capacity of channels.

Entangled photon pairs can alternatively be generated from other sources based on $\chi^{(2)}$ nonlinearity. Planar (rectangular) periodically-poled waveguides made of PPKPT or LiNbO₃ [31–34] represent well-developed and highly-efficient photon-pair sources. However, their mode profiles reflect their rectangular transverse profiles that cannot be easily and effectively transformed into modes of fibers. On the other hand, there exist structured photonic waveguides with eigenmodes close to OAM modes [27, 28]. Unfortunately, these fibers have transverse profiles typically few tens of micrometers wide and so they are not suitable for thermal poling. Thus, the investigated ring shaped fibers, though only weakly nonlinear [35], may provide an interesting solution to the problem. Also the weakness of nonlinear interaction may partly be compensated by the fiber length.

OAM fields are beneficial for both the classical and quantum areas of physics. Sufficiently strong (classical) fields are namely useful for nano-particle manipulations [36]. From the point of view of quantum communications that use individual photon pairs, entangled states are crucial. As we show below, the process of SPDC in the thermally poled fibers discussed above allows to generate photon pairs entangled in different degrees of freedom. These fibers then represent sources of entangled photons that can be directly integrated into optical fiber networks [35]. We note that entanglement in OAM numbers offers additional advantage for the construction division multiplexing systems [29]. OAM multi/demultiplexers have been recently addressed in [37]. Efficiency of these systems has been characterized via the crosstalk between demultiplexed OAM modes (the maximum value equaled -8 dB) and total losses (~ 18 dB). The entangled OAM fields also allow to implement various quantum computation protocols including the above mentioned quantum random walks [38, 39] and a CNOT gate [40]. Last but not least, OAM fields have been found extraordinarily useful in the area of atomic physics where they enable enhanced control of transitions between atomic levels [41].

Photon pairs in fibers can also be generated via the process of four-wave mixing using $\chi^{(3)}$ susceptibility available in usual optical fibers. However, there also occur other competing nonlinear processes based on $\chi^{(3)}$ susceptibility (Raman scattering). Their presence results in larger values of single-photon noise superimposed on photon-pair fields. Despite this, a lot of attention has been devoted to such sources emitting photon pairs both around 800 nm and 1550 nm [42–44].

The paper is organized as follows. In Sec. II, a theoretical model of SPDC in a ring fiber is developed using fiber eigenmodes and propagation constants. Sec. III describes the decomposition into OAM modes and Sec. IV brings analysis of eigenmodes of a ring fiber. Generation of photon pairs with nonzero OAM numbers are discussed in Sec. V. Sec. VI is devoted to the generation of wide-band down-converted fields. Suitable conditions for the generation of photon pairs entangled in OAM states are analyzed in Sec. VII. Also quantification of entanglement of photons in a pair is provided in this section. Sec. VIII brings conclusions.

II. SPONTANEOUS PARAMETRIC DOWN-CONVERSION IN A RING FIBER

Nonlinear process of SPDC occurring among the pump (p), signal (s) and idler (i) fields can be described in general by the following interaction Hamiltonian \hat{H}_{int} [45]:

$$\hat{H}_{\text{int}}(t) = 2\varepsilon_0 \int_{S_{\perp}} r dr d\theta \int_{-L}^0 dz \chi^{(2)}(z) : \mathbf{E}_p^{(+)}(r, \theta, z, t) \times \hat{\mathbf{E}}_s^{(-)}(r, \theta, z, t) \hat{\mathbf{E}}_i^{(-)}(r, \theta, z, t) + \text{h.c.} \quad (1)$$

Symbol $:$ means tensor shorthand with respect to its three indices, ε_0 denotes the vacuum permittivity and h.c. replaces the Hermitian conjugated term. A vector positive-frequency electric-field amplitude of a pump beam is denoted as $\mathbf{E}_p^{(+)}(r, \theta, z, t)$ whereas vector negative-frequency electric-field operator amplitudes of the signal and idler beams are described as $\hat{\mathbf{E}}_s^{(-)}(r, \theta, z, t)$ and $\hat{\mathbf{E}}_i^{(-)}(r, \theta, z, t)$, respectively. Nonlinear susceptibility $\chi^{(2)}$ is assumed z -dependent. Its spatial periodic rectangular modulation along the z axis with certain period permits quasi-phase-matching of the nonlinear process. Hamiltonian \hat{H}_{int} in Eq. (1) is written in cylindrical coordinates with radial variable r , angular variable θ and longitudinal variable z . Symbol S_{\perp} denotes the transverse area of the fiber of length L .

Thermal poling of SiO₂ material giving nonlinearity to the fiber results in the following non-zero elements of $\chi^{(2)}$ tensor: $\chi_{xxx}^{(2)} \simeq 3\chi_{xyy}^{(2)}$ and $\chi_{xyy}^{(2)} = \chi_{yyx}^{(2)} = \chi_{yxy}^{(2)} = 0.021$ pm/V [16, 46]. These values of $\chi^{(2)}$ nonlinearity are approx. three orders in magnitude lower than those characterizing LiNbO₃, the most-frequently used nonlinear material ($\chi^{(2)} \approx 30$ pm/V). On the other hand, sufficiently long fibers allow, at least partially, to compensate the weak nonlinearity [26]. Also, optical fibers profit from the transverse confinement of the guided fields. It is important to note that the ring fibers partially loose their radial symmetry owing to the presence of two thin metallic wires used for thermal poling. However, the holes with wires are usually far from the fiber core and so their influence to radial symmetry of fiber modes results in only weak anisotropy that can usually be omitted.

In the considered ring fiber with its rotational symmetry around the z axis, the pump, signal and idler fields can be decomposed into transverse eigenmodes $\mathbf{e}_\eta(r, \theta, \omega)$ with propagation constants $\beta_\eta(\omega)$ at the appropriate frequencies ω . Multi-index η contains a mode name [47] including azimuthal (n) and radial indices and polarization index ϕ . In this decomposition, the strong (classical) positive-frequency electric-field pump amplitude $\mathbf{E}_p^{(+)}$ attains the form

$$\mathbf{E}_p^{(+)}(r, \theta, z, t) = \sum_{\eta_p} A_{p, \eta_p} \int d\omega_p \mathcal{E}_p(\omega_p) \mathbf{e}_{p, \eta_p}(r, \theta, \omega_p) \times \exp[i\beta_{p, \eta_p}(\omega_p)z - i\omega_p t], \quad (2)$$

in which A_{p, η_p} gives the amplitude of mode η_p and \mathcal{E}_p stands for the pump normalized amplitude spectrum. As the normalized eigenmodes $\mathbf{e}_\eta(r, \theta, \omega)$ form a basis, they can be used for quantization of the signal- and idler-field photon fluxes [48, 49]. As a consequence, the negative-frequency electric-field signal and idler operator amplitudes $\hat{\mathbf{E}}_s^{(-)}$ and $\hat{\mathbf{E}}_i^{(-)}$ can be expressed as

$$\hat{\mathbf{E}}_a^{(-)}(r, \theta, z, t) = \sum_{\eta_a} \int d\omega_a \sqrt{\frac{\hbar\omega_a}{4\pi\epsilon_0 c \bar{n}_{a, \eta_a}}} \hat{a}_{a, \eta_a}^\dagger(\omega_a) \times \mathbf{e}_{a, \eta_a}^*(r, \theta, \omega_a) \exp[i\beta_{a, \eta_a}(\omega_a)z - i\omega_a t], \quad a = s, i; \quad (3)$$

\hbar is the reduced Planck constant, c speed of light in the vacuum and \bar{n}_{a, η_a} effective index of refraction for mode η_a of field a ($\bar{n}_{a, \eta_a} = c\beta_{a, \eta_a}/\omega_a$). The boson creation operators $\hat{a}_{a, \eta_a}^\dagger(\omega_a)$ in Eq. (3) add one photon into mode a with index η_a and frequency ω_a . We note that the eigenmodes are normalized such that $\int r dr d\theta |\mathbf{e}_{a, \eta_a}(r, \theta, \omega_a)|^2 = 1$.

For the considered ring fiber composed of SiO₂ cladding and SiO₂ core doped by 19.3 mol% of GeO₂ (for the scheme, see Fig. 1) [50, 51], the normalized electric-field eigenmodes $\mathbf{e}_\eta(r, \theta, \omega)$ together with the accompanying normalized magnetic-field eigenmodes $\mathbf{h}_\eta(r, \theta, \omega)$ can be obtained analytically. Their longitudinal z components can be expressed in terms of Bessel functions of the first (J_n) and second (Y_n) kind and modified Bessel functions of the first (I_n) and second (K_n) kind as follows [52]:

$$\begin{aligned} \mathbf{e}_{z, \eta}(r, \theta, \omega) &= \left\{ C_\eta^{(0)}(\omega) I_n(w_\eta^{(0)} r) \text{rect}_{0, r_1}(r) \right. \\ &\quad + \left[C_\eta^{(1)}(\omega) J_n(w_\eta^{(1)} r) + D_\eta^{(1)}(\omega) Y_n(w_\eta^{(1)} r) \right] \text{rect}_{r_1, r_2}(r) \\ &\quad \left. D_\eta^{(2)}(\omega) K_n(w_\eta^{(2)} r) \text{rect}_{r_2, \infty}(r) \right\} \sin(n\theta + \phi), \\ \mathbf{h}_{z, \eta}(r, \theta, \omega) &= \left\{ A_\eta^{(0)}(\omega) I_n(w_\eta^{(0)} r) \text{rect}_{0, r_1}(r) \right. \\ &\quad + \left[A_\eta^{(1)}(\omega) J_n(w_\eta^{(1)} r) + B_\eta^{(1)}(\omega) Y_n(w_\eta^{(1)} r) \right] \text{rect}_{r_1, r_2}(r) \\ &\quad \left. B_\eta^{(2)}(\omega) K_n(w_\eta^{(2)} r) \text{rect}_{r_2, \infty}(r) \right\} \cos(n\theta + \phi). \quad (4) \end{aligned}$$

Function $\text{rect}_{a, b}(r)$ equals 1 for $r \in \langle a, b \rangle$ and is zero otherwise. Whereas the Bessel functions describe the oscillating solutions inside the ring core with higher index of

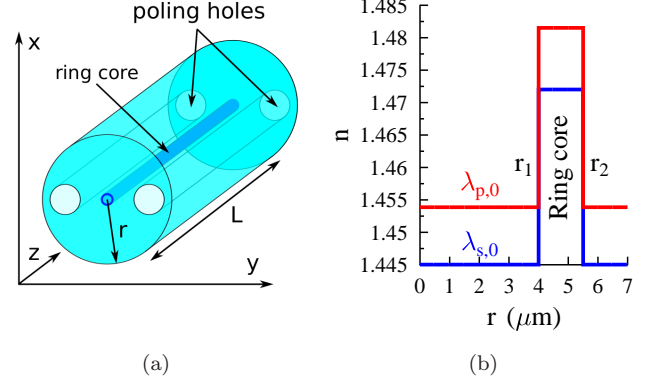


FIG. 1: [Color online:] (a) Sketch of a ring fiber with two small poling holes and (b) radial profiles of indices of refraction n at the pump ($\lambda_p^0 = 0.775 \mu\text{m}$) and signal ($\lambda_s^0 = 1.55 \mu\text{m}$) wavelengths.

refraction extending from $r = r_1$ to $r = r_2$, the modified Bessel functions express the exponentially growing solutions in the center of the fiber and the exponentially decreasing solutions in the outer cladding. Transverse components of the wave vector $w^{(q)}$ introduced in Eqs. (4) are real and they differ according to the radial region:

$$\begin{aligned} w_\eta^{(q)}(\omega) &= \sqrt{\beta_\eta^2(\omega) - \frac{\omega^2}{c^2} \epsilon_r^{(q)}(\omega)}, \quad q = 0, 2, \\ w_\eta^{(1)}(\omega) &= \sqrt{\frac{\omega^2}{c^2} \epsilon_r^{(1)}(\omega) - \beta_\eta^2(\omega)}. \quad (5) \end{aligned}$$

Relative permittivity $\epsilon_r^{(1)}(\omega)$ characterizes the fiber ring core, permittivity $\epsilon_r^{(0)}(\omega)$ describes the fiber inner cladding and permittivity $\epsilon_r^{(2)}(\omega)$ is appropriate for the fiber outer cladding. All permittivities are considered to be scalar quantities. Values of real coefficients $A_\eta^{(0)}(\omega)$, $A_\eta^{(1)}(\omega)$, $B_\eta^{(1)}(\omega)$, $B_\eta^{(2)}(\omega)$, $C_\eta^{(0)}(\omega)$, $C_\eta^{(1)}(\omega)$, $D_\eta^{(1)}(\omega)$, and $D_\eta^{(2)}(\omega)$ occurring in Eqs. (4) are obtained from the requirement of continuity of tangential (θ and z) components of vector electric- [$\mathbf{e}_\eta(r, \theta, \omega)$] and magnetic-field [$\mathbf{h}_\eta(r, \theta, \omega)$] amplitudes at the boundaries of the ring core. This continuity requirement is fulfilled only for specific values of the propagation constant $\beta_\eta(\omega)$ that arise as the solution of dispersion equation [47, 52].

The θ and r components of the electric- and magnetic-field amplitudes are obtained from their z components in Eqs. (4) using the following formulas originating in the

Maxwell equations,

$$\begin{aligned}\mathbf{e}_{r,\eta} &= \frac{c^2}{\varepsilon_r\omega^2 - \beta_\eta^2 c^2} \left[\frac{i\omega\mu_0}{r} \frac{\partial \mathbf{h}_{z,\eta}}{\partial \theta} + i\beta_\eta \frac{\partial \mathbf{e}_{z,\eta}}{\partial r} \right], \\ \mathbf{e}_{\theta,\eta} &= \frac{c^2}{\varepsilon_r\omega^2 - \beta_\eta^2 c^2} \left[-i\omega\mu_0 \frac{\partial \mathbf{h}_{z,\eta}}{\partial r} + \frac{i\beta_\eta}{r} \frac{\partial \mathbf{e}_{z,\eta}}{\partial \theta} \right], \\ \mathbf{h}_{r,\eta} &= \frac{c^2}{\varepsilon_r\omega^2 - \beta_\eta^2 c^2} \left[-\frac{i\omega\varepsilon_0\varepsilon_r}{r} \frac{\partial \mathbf{e}_{z,\eta}}{\partial \theta} + i\beta_\eta \frac{\partial \mathbf{h}_{z,\eta}}{\partial r} \right], \\ \mathbf{h}_{\theta,\eta} &= \frac{c^2}{\varepsilon_r\omega^2 - \beta_\eta^2 c^2} \left[i\omega\varepsilon_0\varepsilon_r \frac{\partial \mathbf{e}_{z,\eta}}{\partial r} + \frac{i\beta_\eta}{r} \frac{\partial \mathbf{h}_{z,\eta}}{\partial \theta} \right].\end{aligned}\quad (6)$$

Alternatively, the θ and r components can be replaced by the cartesian x and y components obtained by the simple relations:

$$\begin{aligned}\mathbf{e}_{x,\eta}(r, \theta, \omega) &= \cos(\theta)\mathbf{e}_{r,\eta}(r, \theta, \omega) - \sin(\theta)\mathbf{e}_{\theta,\eta}(r, \theta, \omega), \\ \mathbf{e}_{y,\eta}(r, \theta, \omega) &= \sin(\theta)\mathbf{e}_{r,\eta}(r, \theta, \omega) + \cos(\theta)\mathbf{e}_{\theta,\eta}(r, \theta, \omega).\end{aligned}\quad (7)$$

The electric- and magnetic-field amplitudes for azimuthal index $n \neq 0$ in Eqs. (4) also depend on phase ϕ that determines the mode polarization. An eigenmode with vertical (horizontal) polarization V (H) is obtained for $\phi = 0$ ($\phi = \pi/2$). As pairs of eigemodes with V and H polarizations have the same propagation constant β_η , eigenmodes with right- (R) and left-handed (L) circular polarizations can be built from these eigemodes using the relations:

$$\begin{aligned}\mathbf{e}_{z,\tilde{\eta}R}(r, \theta, \omega) &= \frac{1}{\sqrt{2}} [\mathbf{e}_{z,\tilde{\eta}V}(r, \theta, \omega) - i\mathbf{e}_{z,\tilde{\eta}H}(r, \theta, \omega)], \\ \mathbf{e}_{z,\tilde{\eta}L}(r, \theta, \omega) &= \frac{1}{\sqrt{2}} [\mathbf{e}_{z,\tilde{\eta}V}(r, \theta, \omega) + i\mathbf{e}_{z,\tilde{\eta}H}(r, \theta, \omega)],\end{aligned}\quad (8)$$

where $\tilde{\eta}$ indicates a mode excluding its polarization. These eigemodes are close to OAM eigemodes and in general possess nonzero OAM numbers. The electric- and magnetic-field amplitudes for $n = 0$ in Eqs. (4) describe two orthogonal TE₀₁ and TM₀₁ eigenmodes with different propagation constants $\beta_\eta(\omega)$. Polarization of TE₀₁ [TM₀₁] mode is obtained for $\phi = 0$ [$\phi = \pi/2$].

A common state $|\psi\rangle$ of the signal and idler fields at the output face of the fiber describing one photon pair is determined by a first-order perturbation solution of the Schrödinger equation with the interaction Hamiltonian \hat{H}_{int} ,

$$|\psi\rangle = -\frac{i}{\hbar} \int_{-\infty}^{\infty} dt \hat{H}_{\text{int}}(t) |\text{vac}\rangle. \quad (9)$$

State $|\text{vac}\rangle$ denotes the vacuum state.

Substitution of the expressions from Eqs. (1–3) into Eq. (9) provides the output state $|\psi\rangle$ in the form:

$$\begin{aligned}|\psi\rangle &= \sum_{\eta_p} \sum_{\eta_s, \eta_i} \int d\omega_s \int d\omega_i \Phi_{\eta_s \eta_i}^{\eta_p}(\omega_s, \omega_i) \\ &\quad \times \hat{a}_{s, \eta_s}^\dagger(\omega_s) \hat{a}_{i, \eta_i}^\dagger(\omega_i) |\text{vac}\rangle.\end{aligned}\quad (10)$$

Two-photon spectral amplitudes $\Phi_{\eta_s \eta_i}^{\eta_p}(\omega_s, \omega_i)$ introduced in Eq. (10) give a probability amplitude of generating a signal photon into mode η_s with frequency ω_s together with an idler photon into mode η_i with frequency ω_i from a pump photon in mode η_p . They are derived as follows:

$$\Phi_{\eta_s \eta_i}^{\eta_p}(\omega_s, \omega_i) = -\frac{i\sqrt{\omega_s \omega_i}}{\sqrt{\tilde{n}_{s, \eta_s} \tilde{n}_{i, \eta_i}} c} A_{p, \eta_p} \mathcal{E}_p(\omega_s + \omega_i) I_{\eta_s \eta_i}^{\eta_p}(\omega_s, \omega_i), \quad (11)$$

where

$$\begin{aligned}I_{\eta_s \eta_i}^{\eta_p}(\omega_s, \omega_i) &= \sqrt{2\pi} \int_{S_\perp} r dr d\theta \tilde{\chi}^{(2)} [-\Delta\beta_{\eta_s \eta_i}^{\eta_p}(\omega_s, \omega_i)] \\ &\quad : \mathbf{e}_{p, \eta_p}(r, \theta, \omega_s + \omega_i) \mathbf{e}_{s, \eta_s}^*(r, \theta, \omega_s) \mathbf{e}_{i, \eta_i}^*(r, \theta, \omega_i)\end{aligned}\quad (12)$$

and $\Delta\beta_{\eta_s \eta_i}^{\eta_p}(\omega_s, \omega_i) = \beta_{p, \eta_p}(\omega_s + \omega_i) - \beta_{s, \eta_s}(\omega_s) - \beta_{i, \eta_i}(\omega_i)$ characterizes phase mismatch of the nonlinear interaction.

Fourier transform $\tilde{\chi}^{(2)}(\beta)$ of spatially modulated $\chi^{(2)}(z)$ nonlinearity used in Eq. (12) is given as follows:

$$\tilde{\chi}^{(2)}(\beta) = \frac{1}{\sqrt{2\pi}} \int_{-\infty}^{\infty} dz \chi^{(2)}(z) \exp(-i\beta z). \quad (13)$$

It attains the following form for the considered rectangular modulation composed of $2N + 1$ periods of length λ [$L = (2N + 1)\Lambda$]:

$$\begin{aligned}\tilde{\chi}^{(2)}(\beta) &= \chi^{(2)} \frac{2}{\sqrt{2\pi}\beta} \sin(\beta\Lambda/4) \frac{\sin[(N + 1/2)\beta\Lambda]}{\sin(\beta\Lambda/2)} \\ &\quad \times \exp(i\beta\Lambda/4) \exp(iN\beta\Lambda).\end{aligned}\quad (14)$$

Photon-pair number density $N_{\eta_s \eta_i}^{\eta_p}(\omega_s, \omega_i)$ belonging to an individual nonlinear process (η_p, η_s, η_i) is defined as

$$N_{\eta_s \eta_i}^{\eta_p}(\omega_s, \omega_i) = \langle \psi | \hat{a}_{s, \eta_s}^\dagger(\omega_s) \hat{a}_{i, \eta_i}^\dagger(\omega_i) \hat{a}_{s, \eta_s}(\omega_s) \hat{a}_{i, \eta_i}(\omega_i) | \psi \rangle. \quad (15)$$

Using Eq. (10), the density $N_{\eta_s \eta_i}^{\eta_p}$ can be expressed in a simple form:

$$N_{\eta_s \eta_i}^{\eta_p}(\omega_s, \omega_i) = |\Phi_{\eta_s \eta_i}^{\eta_p}(\omega_s, \omega_i)|^2. \quad (16)$$

The corresponding signal photon-number density $N_{s, \eta_s}^{\eta_p}(\omega_s)$ is then derived according to the formula

$$N_{s, \eta_s}^{\eta_p}(\omega_s) = \int d\omega_i N_{\eta_s \eta_i}^{\eta_p}(\omega_s, \omega_i). \quad (17)$$

Whereas the two-photon amplitudes $\Phi(\omega_s, \omega_i)$ defined in Eq. (11) characterize the emitted photon pair in spectral domain, temporal two-photon amplitudes $\tilde{\Phi}(t_s, t_i)$ defined as [53]

$$\tilde{\Phi}(t_s, t_i) = \langle \text{vac} | \hat{E}_s^{(+)}(0, t_s) \hat{E}_i^{(+)}(0, t_i) | \psi \rangle \quad (18)$$

are useful for the description of photon pairs in time domain. The substitution of Eqs. (3) and (10) into Eq. (18) gives us the formula valid outside the fiber:

$$\begin{aligned}\tilde{\Phi}_{\eta_s \eta_i}^{\eta_p}(t_s, t_i) &= \frac{\hbar}{4\pi\varepsilon_0 c} \int d\omega_s \int d\omega_i \frac{\sqrt{\omega_s \omega_i}}{\sqrt{\tilde{n}_{s, \eta_s} \tilde{n}_{i, \eta_i}}} \\ &\quad \times \Phi_{\eta_s \eta_i}^{\eta_p}(\omega_s, \omega_i) \exp(-i\omega_s t_s) \exp(-i\omega_i t_i).\end{aligned}\quad (19)$$

Photon pairs generated in an individual nonlinear process (η_p, η_s, η_i) usually have a complex spectral structure that can be revealed by the Schmidt decomposition of spectral two-photon amplitude $\Phi_{\eta_s \eta_i}^{\eta_p}$,

$$\Phi_{\eta_s \eta_i}^{\eta_p}(\omega_s, \omega_i) = \sum_{k=0}^{\infty} \lambda_{\omega, k} f_{s, k}(\omega_s) f_{i, k}(\omega_i). \quad (20)$$

In Eq. (20), functions $f_{s, k}$ and $f_{i, k}$ form a Schmidt dual basis and eigenvalues $\lambda_{\omega, k}$ give coefficients of the decomposition. Provided that these coefficients are properly normalized ($\sum_{k=0}^{\infty} \lambda_{\omega, k}^2 = 1$) they determine the Schmidt number K_ω of independent modes needed in the description [54],

$$K_\omega = \frac{1}{\sum_{k=0}^{\infty} \lambda_{\omega, k}^4}. \quad (21)$$

III. OAM DECOMPOSITION OF MODES IN THE TRANSVERSE PLANE

Vector modes in the transverse plane have in general a complex structure that, however, has to accord with rotational symmetry of the fiber. For this reason, it is useful to decompose their azimuthal dependencies into eigenmodes of OAM operator $\hat{L}(\theta)$, $\hat{L}(\theta) = -i\hbar\partial/(\partial\theta)$, that take the form of harmonic functions [55]:

$$t_l(\theta) = \frac{1}{\sqrt{2\pi}} \exp(il\theta). \quad (22)$$

Convenience of this decomposition is even emphasized when nonlinear processes are taken into account as there occurs the conservation law of OAM number l [56]. This law immediately follows from the integration over azimuthal angle θ in the interaction Hamiltonian \hat{H}_{int} written in Eq. (1). For the considered SPDC process, this law is expressed as

$$l_p = l_s + l_i, \quad (23)$$

where the subscripts indicate the participating fields.

The electric-field modes $\mathbf{e}_\eta(r, \theta, \omega)$ involved in the interactions are vectorial, but their longitudinal components $\mathbf{e}_{z, \eta}(r, \theta, \omega)$ are usually at least one order of magnitude smaller compared to their transverse components $\mathbf{e}_{r, \eta}(r, \theta, \omega)$, $\mathbf{e}_{\theta, \eta}(r, \theta, \omega)$ or $\mathbf{e}_{x, \eta}(r, \theta, \omega)$, $\mathbf{e}_{y, \eta}(r, \theta, \omega)$ [47, 52]. For this reason, we concentrate our attention to the analysis of transverse components. The analysis of cartesian transverse components $\mathbf{e}_{x, \eta}(r, \theta, \omega)$ and $\mathbf{e}_{y, \eta}(r, \theta, \omega)$ is more useful as they can easily be experimentally obtained using optical polarizers. Moreover, the x and y components of electric-field amplitude $\mathbf{e}_\eta(r, \theta, \omega)$ of the circularly polarized modes given in Eq. (8) are only mutually shifted in azimuthal variable θ by $\pi/2$. That is why, we further pay attention only to the x component $\mathbf{e}_{x, \eta}(r, \theta, \omega) \equiv e_\eta(r, \theta, \omega)$.

The mode functions $e_\eta(r, \theta, \omega)$ depend in general on three variables r , θ and frequency ω . Following the rules of quantum mechanics, the probability p of detecting a photon in an OAM eigenstate t_l is given by the formula [55]:

$$p_{l, \eta}(\omega) = \int r dr \left| \int d\theta t_l^*(\theta) e_\eta(r, \theta, \omega) \right|^2 \quad (24)$$

that expresses averaging over the radial variable r .

As entangled photon pairs in their general form (for hyper-entangled photons, see [57, 58]) are emitted, two-photon amplitudes Φ depending on both transverse-plane variables and frequencies are needed in their description. They generalize the two-photon spectral amplitudes $\Phi_{\eta_s \eta_i}^{\eta_p}(\omega_s, \omega_i)$ defined in Eq. (11). In the usually considered spectral ranges several nm wide, the two-photon amplitude $\Phi(r_s, \theta_s, \omega_s, r_i, \theta_i, \omega_i)$ can be approximately written in the following factorized form:

$$\Phi(r_s, \theta_s, \omega_s, r_i, \theta_i, \omega_i) \approx \Phi_{r\theta}(r_s, \theta_s, r_i, \theta_i) \Phi_\omega(\omega_s, \omega_i). \quad (25)$$

The transverse part $\Phi_{r\theta}$ of two-photon amplitude can in principle be decomposed similarly as the spectral part Φ_ω in Eq. (18), i.e.

$$\Phi_{r\theta}(r_s, \theta_s, r_i, \theta_i) = \sum_m \lambda_{r\theta, m} g_{s, m}(r_s, \theta_s) g_{i, m}(r_i, \theta_i) \quad (26)$$

using eigenvalues $\lambda_{r\theta, m}$ and eigenfunctions $g_{s, m}$ and $g_{i, m}$. The eigenvalues $\lambda_{r\theta, m}$ then determine the Schmidt number $K_{r\theta}$ of independent modes by the formula (21). However, the decomposition (26) is usually difficult to achieve. Nevertheless, the two-photon amplitude $\Phi_{r\theta}(r_s, \theta_s, r_i, \theta_i)$ nearly factorizes into its radial and azimuthal parts due to a simple radial dependence in our case. Then we can obtain an approximate number K_θ of modes from singular values $\lambda_{\theta, l}$ of matrix F_θ defined as

$$F_{\theta, l_s l_i} = \left[\int r_s dr_s \int r_i dr_i \left| \int d\theta_s \int d\theta_i t_{l_s}^*(\theta_s) t_{l_i}^*(\theta_i) \Phi_{r\theta}(r_s, \theta_s, r_i, \theta_i) \right|^2 \right]^{1/2} \quad (27)$$

using Eq. (21).

IV. GUIDED MODES OF A RING FIBER

We consider the generation of photon pairs around the wavelengths λ_s^0 and λ_i^0 equal to $1.55 \mu\text{m}$ using the pump field at the wavelength $\lambda_p^0 = 0.775 \mu\text{m}$. From the considerations of fields' propagation stability and efficiency of the nonlinear interaction, the fiber was designed to guide radial fundamental modes for wavelengths longer than $1.2 \mu\text{m}$. This can be assured by a suitable choice

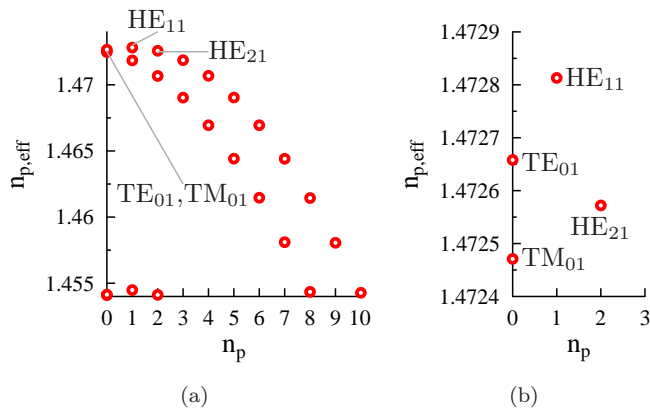


FIG. 2: (a) Effective refractive index $n_{p,\text{eff}}$ of the pump field in dependence on azimuthal number n_p for $\lambda_p^0 = 0.775 \mu\text{m}$. In (b), detail of the graph around $n_p = 0$ is shown.

of geometry of the fiber. It holds that the fundamental mode arises as the first solution of dispersion equation with the highest value of propagation constant $\beta(\omega)$ and occurs even at the lowest possible guided frequencies. Higher-order modes given by subsequent solutions of the dispersion equation exist in general only for higher frequencies ω . The higher the radial mode number, the higher the threshold frequency ω . This property allows us to exclude higher-order modes for the chosen frequencies (wavelengths) by a suitable choice of radii r_1 and r_2 of the fiber ring core (Fig. 1). Detailed numerical calculations have revealed that the analyzed fiber with its core extending from $r_1 = 4 \mu\text{m}$ to $r_2 = 5.5 \mu\text{m}$ admits only the radial fundamental modes for the wavelengths longer than $1.2 \mu\text{m}$.

Effective indices of refraction $n_{p,\text{eff}}$ ($n_{p,\text{eff}} = c\beta_p/\omega_p$) for the pump field at the wavelength $\lambda_p^0 = 0.775 \mu\text{m}$ are shown in Fig. 2. They can be indexed by two numbers, the first counts azimuthal modes and the second radial modes in cylindrical coordinates. The higher the value of the index number, the more complex the mode transverse profile. Modes with the simplest transverse profiles are interesting for the nonlinear interaction as they propagate with low distortions and also allow to reach the greatest values of the interaction overlap integral written in Eq. (12). From this point of view, TE_{01} , TM_{01} , HE_{11} , and HE_{21} modes with the greatest effective indices of refraction $n_{p,\text{eff}}$ are important (see Fig. 2). Whereas transverse components of TE_{01} and TM_{01} modes have a complex structure from the point of view of OAM eigenmodes $t_l(\theta)$ given by Eq. (22), transverse components of modes $\text{HE}_{11,R}$ and $\text{HE}_{11,L}$ are close to eigenmode $t_0(\theta)$. Transverse components of mode $\text{HE}_{21,R}$ [$\text{HE}_{21,L}$] are close to eigenmode $t_{+1}(\theta)$ [$t_{-1}(\theta)$] and so bear a nonzero OAM (for details, see Fig. 4 below).

The signal and idler fields analyzed at the wavelength $\lambda_s^0 = \lambda_i^0 = 1.55 \mu\text{m}$ contain only radial fundamental modes which effective indices of refraction $n_{s,\text{eff}}$ are plot-

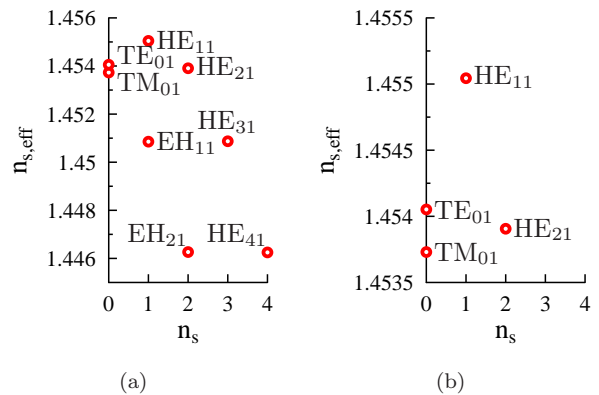


FIG. 3: (a) Effective refractive index $n_{s,\text{eff}}$ of the signal field in dependence on azimuthal number n_s for $\lambda_s^0 = 1.55 \mu\text{m}$. In (b), detail of the graph around $n_s = 0$ is shown.

ted in Fig. (3). In total 14 modes occur in the analyzed spectral region: TE_{01} and TM_{01} modes without a defined OAM and both left- and right-handed circularly polarized modes HE_{11} ($l = 0$), HE_{21} ($l = \pm 1$), HE_{31} ($l = \pm 2$), HE_{41} ($l = \pm 3$), EH_{11} ($l = \pm 2$) and EH_{21} ($l = \pm 3$).

Profiles of the x and z components of signal electric-field amplitudes $\mathbf{e}_\eta(r, \theta)$ for four simplest modes, TE_{01} , TM_{01} , HE_{11} , and HE_{21} , are shown in Fig. 4. The y components of electric-field amplitudes $\mathbf{e}_\eta(r, \theta)$ have the same amplitudes as the x components of $\mathbf{e}_\eta(r, \theta)$ but their phases are shifted by $\pi/2$ with respect to the phases of the x components. We note that the pump modes have similar profiles as the signal modes, they are only more localized inside the core ring as a consequence of their half wavelength relative to the signal one.

The weights of individual OAM eigenmodes in the above modes determined by probabilities p in Eq. (24) are important for judging efficiency of the nonlinear interaction as it obeys the conservation law of OAM expressed in Eq. (23). The probabilities p determined for the most useful modes TE_{01} , TM_{01} , HE_{11} , and HE_{21} of the signal field are depicted in Fig. 5. Whereas several OAM eigenmodes are essential for building TE_{01} and TM_{01} modes, the OAM eigenmode $t_0(\theta)$ [$t_{+1}(\theta)$ and $t_{-1}(\theta)$] dominates in the x and y components of electric-field amplitude $\mathbf{e}_\eta(r, \theta)$ of modes $\text{HE}_{11,R}$ and $\text{HE}_{11,L}$ [$\text{HE}_{21,R}$ and $\text{HE}_{21,L}$]. On the other hand, the z components of electric-field amplitudes $\mathbf{e}_\eta(r, \theta)$ usually contain OAM eigenmodes t_l with l in absolute value greater by one compared to their x and y components. So the component $\mathbf{e}_{z,\text{HE}_{m1,R}}(r, \theta)$ [$\mathbf{e}_{z,\text{HE}_{m1,L}}(r, \theta)$] is formed by OAM eigenstate $t_{+m}(\theta)$ [$t_{-m}(\theta)$] for $m = 1, 2$.

These modes of the pump, signal and idler fields can be combined in several different ways in order to arrive at an efficient nonlinear interaction among individual modes. This interaction is efficient provided that the conservation laws of energy and OAM together with quasi-phase-matching are fulfilled. Period Λ of periodical poling is

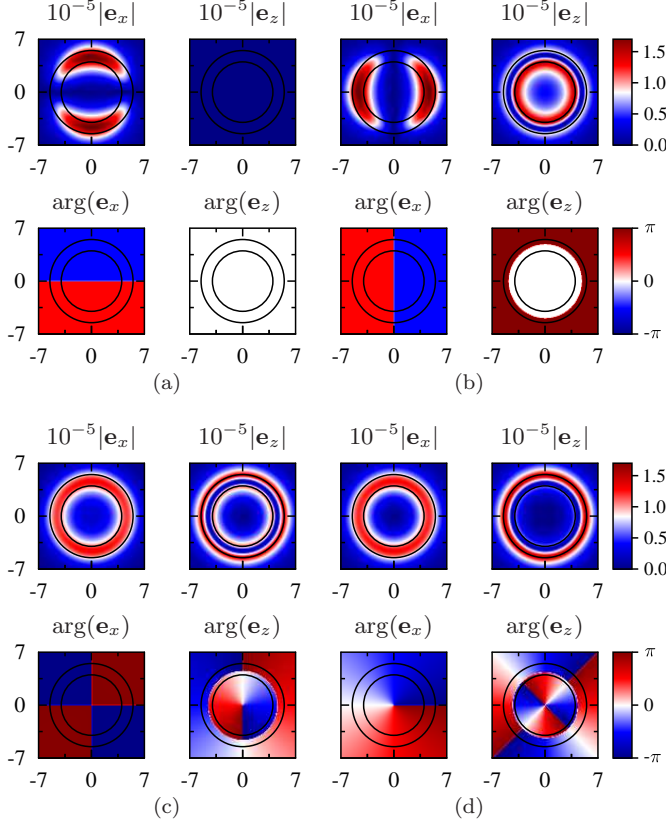


FIG. 4: [Color online:] Amplitude and phase of components $\mathbf{e}_x(x, y)$ and $\mathbf{e}_z(x, y)$ of electric-field amplitudes for modes TE_{01} (a), TM_{01} (b), $\text{HE}_{11,R}$ (c), and $\text{HE}_{21,R}$ (d) for the signal field at $\lambda_s^0 = 1.55 \mu\text{m}$; $x = r \cos(\theta)$, $y = r \sin(\theta)$. The cartesian x and y axes' labels are in μm and the components are normalized according to $\int dx dy |\mathbf{e}_{x,z}(x, y)|^2 = 1$.

the only free parameter that allows us to choose among several individual nonlinear processes. In the following three sections, we analyze different processes that give us both spectrally narrow- and broad-band photon pairs as well as photon pairs entangled in OAM numbers.

V. GENERATION OF PHOTON PAIRS WITH NONZERO OAM NUMBERS

Pump modes with zero OAM numbers l_p are suitable for the generation of spectrally broad-band photon pairs whereas pump modes with non-zero OAM are optimal for the emission of spectrally narrow-band photon pairs. When the conservation law of OAM in Eq. (23) is applied to pump modes $\text{HE}_{11,R}$ and $\text{HE}_{11,L}$ with $l_p = 0$, the signal l_s and idler l_i OAM numbers have to have the same absolute value. The signal and idler modes then naturally have similar properties, which allow for a broad-band photon-pair generation (see the next section). On the other hand, if the pump beam is in mode $\text{HE}_{21,R}$ with $l_p = +1$ (or its left-handed circularly polar-

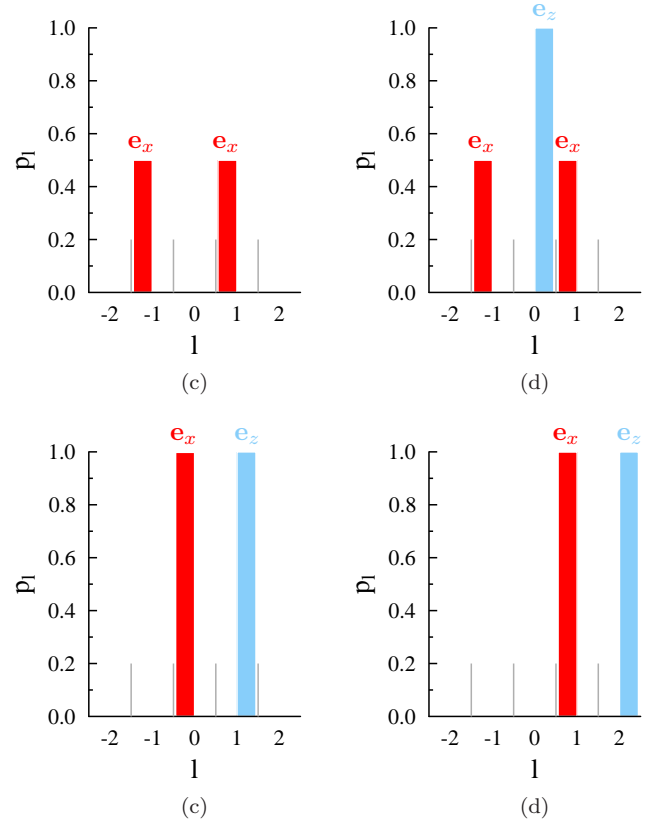


FIG. 5: [Color online:] Probabilities p_l of measuring an OAM eigenmode t_l for the x and z components of electric-field amplitude $\mathbf{e}_\eta(r, \theta, \omega)$ for modes TE_{01} (a), TM_{01} (b), $\text{HE}_{11,R}$ (c), and $\text{HE}_{21,R}$ (d) for the signal field at $\lambda_s^0 = 1.55 \mu\text{m}$.

ized variant $\text{HE}_{21,L}$ with $l_p = -1$) the conservation law of OAM suggests the signal and idler modes with different OAMs. The down-converted modes are then expected to have different properties and the emission of photon-pairs is assumed to be narrow-band and non-degenerate. Stability of the pump mode $\text{HE}_{21,R}$ follows from the graph in Fig. 2 that identifies modes TE_{01} and TM_{01} as the closest modes with respect to effective refractive index $n_{p,\text{eff}}$. However, differences $\Delta n_{p,\text{eff}}$ between the modes ($\Delta n_{p,\text{eff}} = -9 \times 10^{-5}$ for mode TE_{01} , $\Delta n_{p,\text{eff}} = 1 \times 10^{-4}$ for mode TM_{01}) are high enough to guarantee stable guiding of mode HE_{21} without crosstalk.

The signal and idler modes fulfilling the conservation of OAM together with the pump $\text{HE}_{21,R}$ mode are summarized in Tab. I. However, only the variants with the signal $\text{HE}_{21,R}$ mode and idler $\text{HE}_{11,R}$ and $\text{HE}_{11,L}$ modes are sufficiently stable. The fundamental modes $\text{HE}_{11,R}$ and $\text{HE}_{11,L}$ are the most stable. In detail, the difference $\Delta n_{s,\text{eff}}$ of refraction indices of modes HE_{11} and the closest mode TE_{01} equals 1×10^{-3} , whereas $\Delta n_{s,\text{eff}}$ for mode HE_{21} and the closest mode TE_{01} is 1.5×10^{-4} .

Also the signal TE_{01} and TM_{01} modes may participate in the nonlinear interaction as they are partially composed of OAM eigenmodes with $l_s = +1$ (see Fig. 6).

pump	HE _{21,R}		
l_p	+1		
signal	HE _{21,R}	HE _{31,R} EH _{11,R}	HE _{41,R} EH _{21,R}
l_s	1	2	3
idler	HE _{11,R} HE _{11,L}	HE _{21,L}	HE _{31,L} EH _{11,L}
l_i	0	-1	-2

TABLE I: Possible combinations of pump, signal and idler modes with their OAM numbers l (in the weakly-guiding approximation [52]) fulfilling the conservation of OAM.

However, these modes are not suitable for transmission of photons as they do not have a well defined OAM. They can be spectrally separated from the combinations of modes discussed above owing to different propagation constants. They lead to different values of nonlinear phase mismatch $\Delta\beta$ for the considered individual nonlinear processes (HE₂₁^p, HE₂₁^s, HE₁₁ⁱ), (HE₂₁^p, TE₀₁^s, HE₁₁ⁱ) and (HE₂₁^p, TM₀₁^s, HE₁₁ⁱ). The dependence of nonlinear phase mismatch $\Delta\beta$ on signal wavelength λ_s for cw pumping plotted in Fig. 6 shows that a sufficiently narrow spatial spectrum $\tilde{\chi}^{(2)}$ of QPM grating [see Eq. (14)] provides spectral separation of different nonlinear processes. Width $\Delta\tilde{\chi}^{(2)}$ of spatial spectrum can easily be varied by the length L of the grating. The longer the grating, the narrower the spectrum $\tilde{\chi}^{(2)}$ and also the narrower the signal- and idler-field spectra. Individual nonlinear processes are thus better separated for longer QPM gratings. Therefore a suitable length of the grating has to be found. A 10-cm long rectangular grating with period $\Lambda = 42.9 \mu\text{m}$ available by a simple fabrication method [2] (see Fig. 6 for its spectrum $\tilde{\chi}^{(2)}$) satisfies the requirement. It allows the generation of signal photons around the wavelength $\lambda_s^0 = 1.5 \mu\text{m}$ accompanied by idler photons around the wavelength $\lambda_i^0 = 1.6 \mu\text{m}$ in the nonlinear process (HE₂₁^p, HE₂₁^s, HE₁₁ⁱ). Intensity spectral width $\Delta\tilde{\chi}^{(2)}$ equals $2 \times 10^{-4} \mu\text{m}^{-1}$ (full width at half maximum, FWHM) for this grating and guarantees the amount of unwanted photons at the level of 1%.

The number of generated photon pairs depends on the overlap integral containing the product of pump, signal and idler electric-field amplitudes in the transverse plane [see Eq. (12)]. The value of this integral in the azimuthal angle is maximized due to the conservation of OAM. The maximal available value of this integral then depends on radial mode profiles that are shown in Fig. 7 for the chosen nonlinear process. It holds in general that the lower the number of minima in radial intensity profiles, the greater the number of generated photon pairs. This favors modes with lower mode numbers.

Six well separated peaks occur in the down-converted field spectrum $N_s(\lambda_s)$ shown in Fig. 8. The most intensive peak at $\lambda_s = 1.5 \mu\text{m}$ belongs to mode HE_{21,R}^s and originates in the nonlinear processes (HE_{21,R}^p, HE_{21,R}^s, HE_{11,L}ⁱ) and (HE_{21,R}^p, HE_{21,R}^s, HE_{11,R}ⁱ).

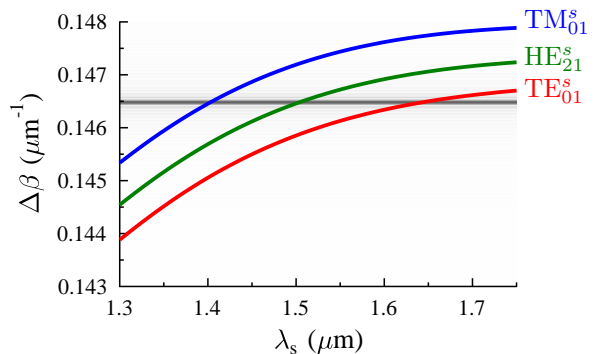


FIG. 6: [Color online:] Phase mismatch $\Delta\beta$ for nonlinear processes (HE₂₁^p, HE₂₁^s, HE₁₁ⁱ), (HE₂₁^p, TE₀₁^s, HE₁₁ⁱ) and (HE₂₁^p, TM₀₁^s, HE₁₁ⁱ). The gray horizontal pattern describes spatial spectrum $\tilde{\chi}^{(2)}(\beta)$ of a rectangular QPM grating with $\Lambda = 42.9 \mu\text{m}$; $L = 10 \text{ cm}$.

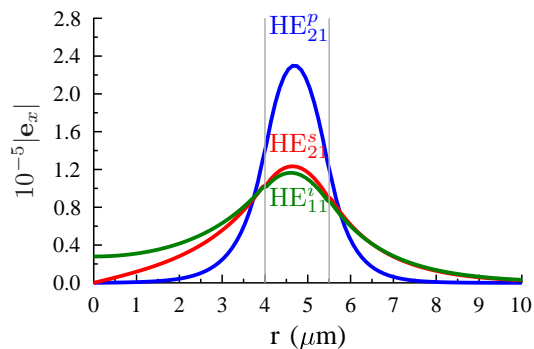


FIG. 7: [Color online:] Absolute value $|e_x|$ of the x component of electric-field amplitude depending on radius r for pump mode HE₂₁^p, signal mode HE₂₁^s and idler mode HE₁₁ⁱ. Normalization is such that $\int dx dy |e_x(x, y)|^2 = 1$.

The accompanying peaks at $\lambda_i = 1.603 \mu\text{m}$ correspond to modes HE_{11,L}ⁱ and HE_{11,R}ⁱ with the same weight. The curves in Fig. 8 confirm that these desired peaks can be well separated by frequency filters from the unwanted ones. We note that the modes HE_{11,L}ⁱ and HE_{11,R}ⁱ with the same spectra cannot be separated and in fact form a common quantum superposition state. The efficiency of spectral separation in ring fibers is similar to that found in nonlinear waveguides with SPDC [59, 60]. Spectral width of the peak at $\lambda_s = 1.5 \mu\text{m}$ equals 9.41 nm (FWHM). The peak occurring at $\lambda_s = 1.4 \mu\text{m}$ belongs to TM₀₁ mode and forms a pair together with the peak at $\lambda_i = 1.73 \mu\text{m}$ given by mode HE_{11,R}ⁱ. Mode TE₀₁ is responsible for the peak at $\lambda_s = 1.63 \mu\text{m}$ that occurs together with the peak at $\lambda_i = 1.47 \mu\text{m}$ established by mode HE_{11,R}ⁱ. We note that small oscillations at the wings of the peaks reflect the shape of spatial spectrum $\tilde{\chi}^{(2)}(\beta)$ of QPM grating.

As follows from Fig. 8, photon-pair density N_s attains

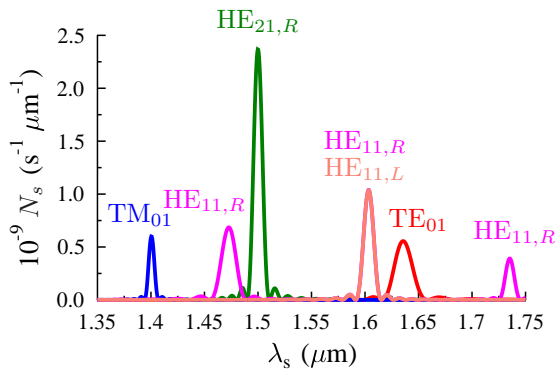


FIG. 8: [Color online:] Spectral photon-number density N_s created by modes $\text{HE}_{21,R}$, $\text{HE}_{11,R}$, $\text{HE}_{11,L}$, TE_{01} , and TM_{01} in dependence on wavelength λ_s ; $N_s(\omega_s) = \sum_{\eta_p, \eta_s, \eta_i} N_{s, \eta_s, \eta_i}^{\eta_p}(\omega_s)$

its maximum value at $2.4 \times 10^9 \text{ nm}^{-1}\text{s}^{-1}$ for 1 W of the pump power. Taking into account the peak spectral width, around 20 photon pairs per 1 s and $1 \mu\text{W}$ of pumping are expected in modes $(\text{HE}_{21,R}^p, \text{HE}_{21,R}^s, \text{HE}_{11}^i)$ provided that appropriate spectral filters are used. The number of generated photon pairs can be increased by considering longer fibers. It can be shown theoretically that the number of photon pairs increases better than linearly with the fiber length. Also narrowing of the emitted spectra occurs with the increasing fiber length. On the other hand, fabrication imperfections as well as non-ideal alignment of the nonlinear interaction in the laboratory reduces these numbers by one or two orders in magnitude [35].

Photon pairs are emitted in states entangled in signal and idler frequencies due to the conservation law of energy. This results in sharp temporal correlations in detection times of the signal and idler photons. For the spectra approx. 10 nm wide, typical entanglement times quantifying these correlations are in hundreds of fs (for details, see Fig. 11 below) [22].

VI. GENERATION OF SPECTRALLY BROAD-BAND PHOTON PAIRS

As it has already been discussed above, the pump field in a $\text{HE}_{11,R}$ (or $\text{HE}_{11,L}$) mode with $l_p = 0$ allows to generate spectrally broad-band photon pairs achievable usually in chirped poled nonlinear materials [18, 61]. This is a consequence of flat spectral dependencies of phase mismatches $\Delta\beta$ of individual nonlinear processes conserving OAM (see Fig. 9). Stable down-converted modes of LP_{11} family, HE_{21} , TE_{01} and TM_{01} , can take part in this interaction. The curves in Fig. 9 indicate that the nonlinear processes $(\text{HE}_{11,R}^p, \text{HE}_{21,R}^s, \text{HE}_{21,L}^i)$, $(\text{HE}_{11,R}^p, \text{HE}_{21,L}^s, \text{HE}_{21,R}^i)$, $(\text{HE}_{11,R}^p, \text{TE}_{01}^s, \text{TM}_{01}^i)$, and $(\text{HE}_{11,R}^p, \text{TM}_{01}^s, \text{TE}_{01}^i)$ occur nearly simultaneously and

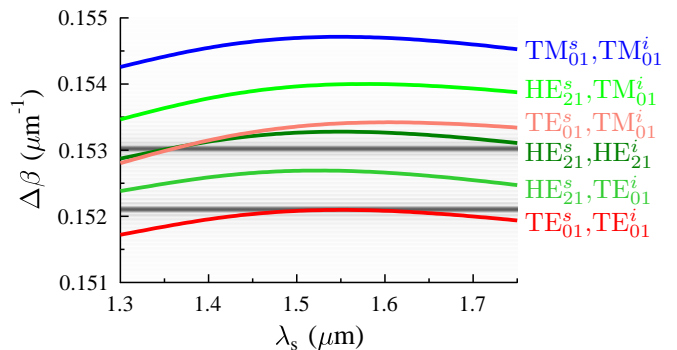


FIG. 9: [Color online:] Phase mismatch $\Delta\beta$ for nonlinear processes pumped by mode $\text{HE}_{11,R}^p$ with signal and idler fields in modes HE_{21} , TE_{01} and TM_{01} in dependence on wavelength of signal photon λ_s . The gray horizontal pattern describes spatial spectra $\tilde{\chi}^{(2)}(\Delta\beta)$ of rectangular nonlinear modulation with $\Lambda = 41.06 \mu\text{m}$ (upper pattern) and $\Lambda = 42.28 \mu\text{m}$ (lower pattern); $L = 10 \text{ cm}$.

thus may provide a more complex state. On the other hand, the processes $(\text{HE}_{11,R}^p, \text{TE}_{01}^s, \text{TE}_{01}^i)$ and $(\text{HE}_{11,R}^p, \text{TM}_{01}^s, \text{TM}_{01}^i)$ can easily be separated from other processes for sufficiently narrow spatial spectra $\tilde{\chi}^{(2)}(\beta)$, similarly as in the case discussed in Sec. V.

As an example, we consider the nonlinear interaction with TE_{01} signal and idler modes. This interaction is achieved for period Λ of the nonlinear modulation equal to $42.28 \mu\text{m}$. Signal photon-number density $N_s(\lambda_s)$ for this process and 10-cm long QPM grating attains its maximum at degenerate wavelength $\lambda_s^0 = 1.55 \mu\text{m}$ where a 142-nm wide peak occurs (FWHM, see Fig. 10). Around 150 photon pairs per 1 s and $1 \mu\text{W}$ of pumping are emitted in this process. The obtained spectrum is approx. 15 times broader compared to that of the process analyzed in Sec. V. This implies considerably sharper temporal features of photon pairs generated by the process $(\text{HE}_{11,R}^p, \text{TE}_{01}^s, \text{TE}_{01}^i)$. Profiles of probability densities $p_{t,i}$ of detecting an idler photon at time t_i conditioned by detection of a signal photon at time $t_s = 0 \text{ s}$ for both cases are compared in Fig. 11 confirming this fact. Whereas the probability-density width equals $4.5 \times 10^{-14} \text{ s}$ (FWHM) for the spectrally broad-band process $(\text{HE}_{11,R}^p, \text{TE}_{01}^s, \text{TE}_{01}^i)$, it attains $63.5 \times 10^{-14} \text{ s}$ for the spectrally narrow-band process $(\text{HE}_{21,R}^p, \text{HE}_{21,R}^s, \text{HE}_{11,R}^i)$. We note that sharp temporal correlations are important in metrology as they determine the available temporal resolution [4, 62].

VII. GENERATION OF PHOTON PAIRS ENTANGLED IN OAM NUMBERS

Pumping the fiber with a $\text{HE}_{11,R}$ (or $\text{HE}_{11,L}$) mode is interesting even in the case when more LP_{11} modes participate in the nonlinear interaction. Period

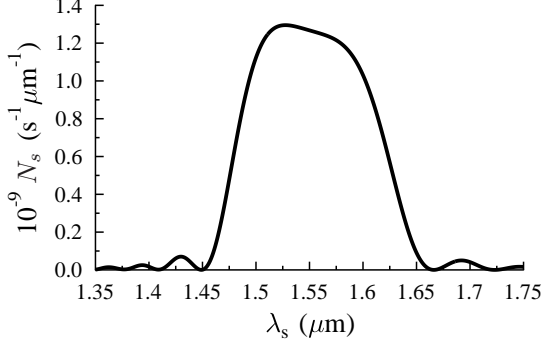


FIG. 10: Spectral photon-number density N_s originating in nonlinear process $(\text{HE}_{11,R}^p, \text{TE}_{01}^s, \text{TE}_{01}^i)$; $\Lambda = 42.28 \mu\text{m}$, $L = 10 \text{ cm}$ in dependence on wavelength λ_s .

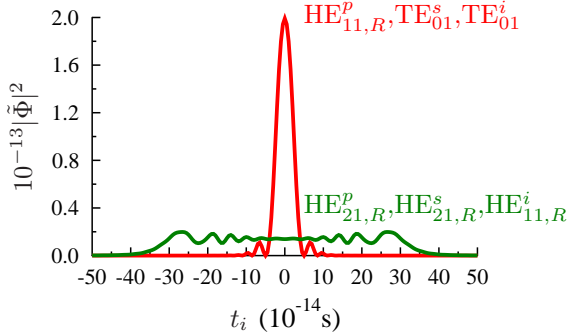


FIG. 11: [Color online:] Probability density $p_{t,i}$, $p_{t,i} = \mathcal{C}|\tilde{\Phi}(0, t_i)|^2$, as a function of idler-photon detection time t_i for a signal photon detected at time $t_s = 0 \text{ s}$ for processes $(\text{HE}_{21,R}^p, \text{HE}_{21,R}^s, \text{HE}_{11,R}^i)$ ($\Lambda = 42.9 \mu\text{m}$) and $(\text{HE}_{11,R}^p, \text{TE}_{01}^s, \text{TE}_{01}^i)$ ($\Lambda = 42.28 \mu\text{m}$), $L = 10 \text{ cm}$. Constant \mathcal{C} is defined such that $\int_{-\infty}^{\infty} dt_i p_{t,i}(t_i) = 1$.

Λ of nonlinear modulation equal to $41.06 \mu\text{m}$ provides suitable conditions for four nonlinear processes $(\text{HE}_{11,R}^p, \text{HE}_{21,R}^s, \text{HE}_{21,L}^i)$, $(\text{HE}_{11,R}^p, \text{HE}_{21,L}^s, \text{HE}_{21,R}^i)$, $(\text{HE}_{21,R}^p, \text{TE}_{01}^s, \text{TM}_{01}^i)$ and $(\text{HE}_{21,R}^p, \text{TM}_{01}^s, \text{TE}_{01}^i)$ (see Fig. 9). The last two processes do not contribute to photon-pair generation as they have zero overlap integrals given in Eq. (12). In the first two nonlinear interactions, the signal and idler photons are generated with OAM numbers equal to ± 1 and ∓ 1 . State $|\psi_{l_s, l_i}\rangle$ entangled in OAM numbers [63] $[|\psi_{l_s, l_i}\rangle = C_1|l_s = 1\rangle_s |l_i = -1\rangle_i + C_2|l_s = -1\rangle_s |l_i = 1\rangle_i$, C_1 and C_2 are constants] can thus be obtained at wavelengths $\lambda_s = 1.35 \mu\text{m}$ and $\lambda_i = 1.82 \mu\text{m}$. As both processes have nearly equal intensities, a generated state close to the maximally entangled state is expected. Also radial profiles of the emitted photons are close to each other which justifies the use of formula (27) for the determination of Schmidt number K_θ . It gives $K_\theta = 1.998$. For comparison, the exact numerical decomposition

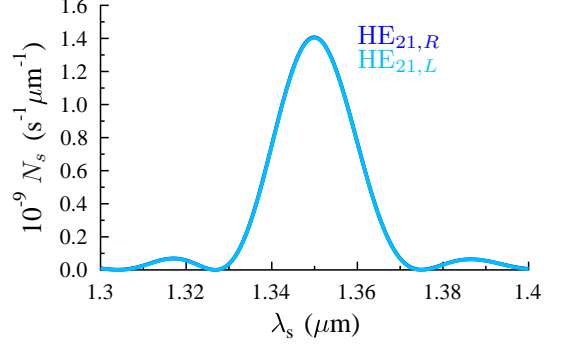


FIG. 12: [Color online:] Spectral photon-number density N_s arising from nonlinear processes $(\text{HE}_{11,R}^p, \text{HE}_{21,R}^s, \text{HE}_{21,L}^i)$ and $(\text{HE}_{11,R}^p, \text{HE}_{21,L}^s, \text{HE}_{21,R}^i)$ in dependence on wavelength λ_s . The curves nearly coincide; $\Lambda = 41.06 \mu\text{m}$, $L = 10 \text{ cm}$.

described in Eq. (26) provides $K_\theta = 1.994$. The obtained peak in the signal photon-number density $N_s(\lambda_s)$ is 21 nm wide (FWHM) and its profile is shown in Fig. 12. The curve plotted in Fig. 12 corresponds to 30 signal photons generated per 1 s and $1 \mu\text{W}$ of pumping, which characterizes an intense source of photon pairs.

The generated state is simultaneously entangled also in the signal and idler frequencies and its state can be expressed as

$$|\psi\rangle = \int d\omega_s d\omega_i \Phi_{1_s, -1_i}(\omega_s, \omega_i) |l_s = 1, \omega_s\rangle_s |l_i = -1, \omega_i\rangle_i + \Phi_{-1_s, 1_i}(\omega_s, \omega_i) |l_s = -1, \omega_s\rangle_s |l_i = 1, \omega_i\rangle_i. \quad (28)$$

We analyze spectral entanglement assuming separability of the spectral profile and that in the transverse plane for both fields. We also analyze the two-photon spectral amplitude $\Phi_{1_s, -1_i}(\omega_s, \omega_i)$ arising from the process $(\text{HE}_{11,R}^p, \text{HE}_{21,R}^s, \text{HE}_{21,L}^i)$ and note that the two-photon amplitude $\Phi_{-1_s, 1_i}(\omega_s, \omega_i)$ of process $(\text{HE}_{11,R}^p, \text{HE}_{21,L}^s, \text{HE}_{21,R}^i)$ is very similar to the former one. As the amount of spectral entanglement depends on the pump-field spectral width σ_p , we consider the Gaussian spectrum \mathcal{E}_p centered at frequency ω_p^0 corresponding to $\lambda_p^0 = 0.775 \mu\text{m}$,

$$\mathcal{E}_p(\omega) = \sqrt{\frac{2}{\pi}} \frac{1}{\sigma_p} \exp\left[-\frac{(\omega - \omega_p^0)^2}{\sigma_p^2}\right]. \quad (29)$$

The two-photon spectral amplitude $\Phi_{1_s, -1_i}(\omega_s, \omega_i)$ considered for a pulsed pump field has a typical elliptical shape with axes oriented at directions $\omega_s = \omega_i - \omega_i^0 + \omega_s^0$ and $\omega_s = \omega_p^0 - \omega_i$. For the analyzed configuration, the pump-field spectrum cannot be wider than $\sigma_p = 0.85 \text{ nm}$ (the corresponding intensity FWHM equals 2 nm) to assure negligible contributions from other nonlinear processes discussed above. In this case, the two-photon amplitude $\Phi_{1_s, -1_i}$ is elongated along the direction $\omega_s = \omega_p^0 - \omega_i$. This is caused by the fact that the extension of

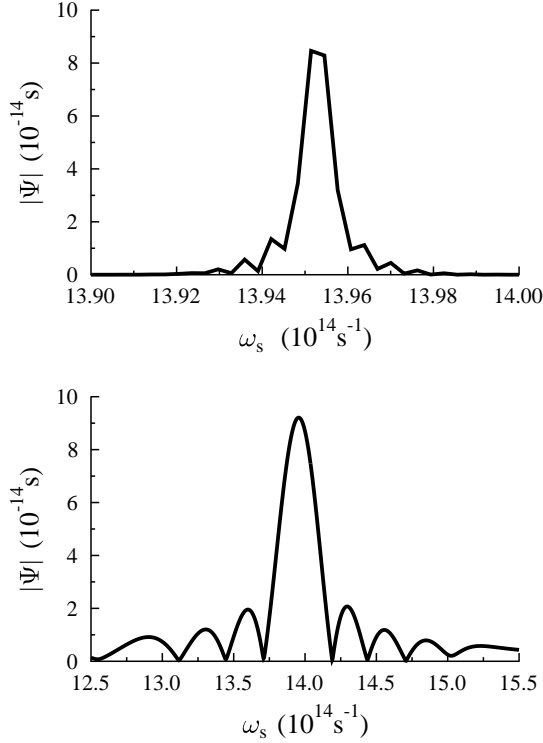


FIG. 13: Cut of absolute value $|\Phi_{1_s, -1_i}(\omega_s, \omega_i)|$ of two-photon spectral amplitude along the line (a) $\omega_s = \omega_i - \omega_i^0 + \omega_s^0$ and (b) $\omega_s = \omega_p^0 - \omega_i$ appropriate for the process $(\text{HE}_{11,R}^p, \text{HE}_{21,R}^s, \text{HE}_{21,L}^i)$ pumped by a pulsed field; $\sigma_p = 0.85$ nm, $\Lambda = 41.06$ μm , $L = 10$ cm. It holds that $\int d\omega_s d\omega_i |\Phi(\omega_s, \omega_i)|^2 = 1$.

amplitude $\Phi_{1_s, -1_i}$ in direction $\omega_s = \omega_i - \omega_i^0 + \omega_s^0$ is limited by the product of pump-field spectrum \mathcal{E}_p and spatial spectrum $\tilde{\chi}^{(2)}$ of nonlinear modulation. As shown in Fig. 13(a) for the pump field with width $\sigma_p = 0.85$ nm, spatial spectrum $\tilde{\chi}^{(2)}$ introduces oscillations in this direction. The extension of amplitude $\Phi_{1_s, -1_i}$ in direction $\omega_s = \omega_p^0 - \omega_i$ depends on phase-matching properties of the structure as well as on the pump-field spectrum. This admits much broader profiles, as documented in Fig. 13(b). Oscillations in spectrum $\tilde{\chi}^{(2)}$ of nonlinear grating are also visible in this profile and reflect profiles of dispersion curves.

There typically occur several tens of independent spectral modes for the considered pulsed pumping. The number K_ω of independent spectral modes determined by formula (21) increases nearly linearly with the increasing pump-field spectral width σ_p in the interval depicted in Fig. 14. This originates in considerable broadening of the signal- and idler-field spectra with the increasing values of spectral width σ_p . The overall number of independent modes is given by the product $K_\theta K_\omega$ of numbers of modes in the spectral and azimuthal variables and thus reaches approx. 200 for the pump field having 0.85-nm wide spectrum. All these modes can, in principle, be used

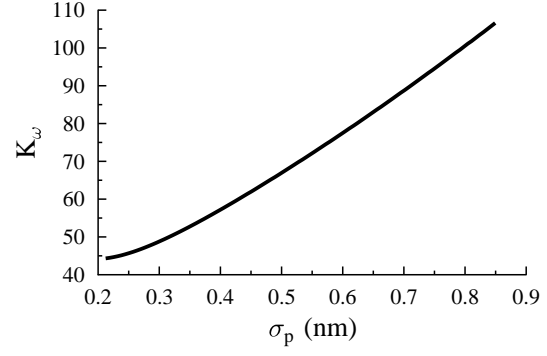


FIG. 14: Number K_ω of independent spectral modes as it depends on pump-field spectral width σ_p ; $\Lambda = 41.06$ μm , $L = 10$ cm.

for quantum communications for delivering entangled information.

We have considered a ring fiber 10 cm long as it can be fabricated by a simple method [25]. However, there exists a more sophisticated fabrication method allowing production of ring fibers up to 1 m long [64]. The numbers of generated photon pairs more than one order of magnitude greater are expected in such fibers.

In many applications, the signal-to-noise ratio of a photon-pair source is an important parameter. In the analyzed ring fiber, we can identify three sources of noise. The first source is related to the presence of other nonlinear processes. As the fiber has losses, one photon from a generated photon pair can be lost leaving the remaining photon in the form of noise. Finally, a photon pair can be emitted into an unwanted pair of modes and so both its photons contribute to the noise. However, it has been shown in [35] that the Raman scattering as well as other nonlinear processes are negligible in regular fibers with the same material structure. As for the broken photon pairs, any measurement based on the detection of photon coincidences eliminates this kind of noise. Our results have shown that the probability of generation of a photon pair into an unwanted pair of modes is lower than 1/100 for the discussed configuration. Thus, all three sources of noise can be neglected.

The discussed noise weakens entanglement of the generated state entangled in OAM numbers. This weakening can be quantified, e.g., using the Clauser-Horne-Shimony-Holt (CHSH) form of the Bell inequalities [65]. To simplify calculations, we first determine a reduced statistical operator $\hat{\rho}_{\text{OAM}}$ corresponding to the state $|\psi\rangle$ in Eq. (28) reduced over the signal (ω_s) and idler (ω_i) frequencies. Considering additional noise with relative weight p , an appropriate statistical operator $\hat{\rho}'_{\text{OAM}}$ can be expressed as

$$\hat{\rho}'_{\text{OAM}} = (1-p)\hat{\rho}_{\text{OAM}} + p\frac{\hat{I}}{4} \quad (30)$$

using the unity operator \hat{I} . Maximal violation of the

CHSH inequalities occurs under conditions discussed in [66]. In this case and assuming $p = 0.01$, parameter S quantifying this violation ($S > 2$) equals 2.8. The boundary value of parameter S ($S = 2$) is observed for $p = 0.283$, which does not represent a real limitation for experiments. For comparison, recent measurements with states entangled in OAM numbers have reached $S = 2.78$ for $l \pm 1$ [67] and $S = 2.69$ for $l \pm 2$ [68].

We note that also vortex fibers have been considered [29] for the propagation of optical fields with nonzero OAM. Compared to ring fibers, they contain an additional central core. As a consequence, their fundamental modes HE_{11} are more stable. This advantage can be exploited also when generating photon pairs as the analysis of SPDC in vortex fibers is similar to that shown here for the ring fibers.

VIII. CONCLUSIONS

A nonlinear thermally-poled ring fiber has been considered as a source of photon pairs arising in the process of spontaneous parametric down-conversion. It has been shown that several combinations of stable pump, signal and idler spatial modes of the fiber are suitable for efficient photon-pair generation depending on the period of $\chi^{(2)}$ modulation introduced into the fiber. Spectrally narrow-band photon pairs in OAM eigenstates emitted

in spectrally separated regions can be achieved this way. Also broad-band photon pairs with spectra more than 100 nm wide can be obtained in the fiber. Even photon-pair states entangled in OAM eigenstates can be generated. For a pulsed pump field with 2-nm wide spectrum (FWHM), combined spectral and azimuthal effective dimensions of the emitted entangled states can reach 200. The considered 10-cm long fiber allows to generate these states with photon-pair fluxes reaching hundreds of pairs per second and μW of pumping. Higher photon-pair fluxes can be obtained from longer fibers. These results show that nonlinear ring and vortex fibers can be designed such that they can emit intensive entangled photon pairs in OAM eigenstates. This is prospective both for quantum communications and optical-fiber-based metrology.

Acknowledgments

The authors thank Juan P. Torres for his advice and discussions as well as hospitality during the stay at ICFO. Support by projects CZ.1.05/2.1.00/03.0058 and CZ.1.07/2.3.00/20.0017 of MŠMT ČR and P205/12/0382 of GA ČR are acknowledged. D.J. and J.P. acknowledge support by project PrF_2013_006 of IGA UP Olomouc. J.S. thanks the projects CZ.1.07/2.3.00/30.0004 and CZ.1.07/2.3.00/20.0058 of MŠMT ČR.

-
- [1] M. A. Nielsen and I. L. Chuang, *Quantum computation and quantum information* (Cambridge University Press, 2010).
 - [2] P. Zhang, X.-F. Ren, X.-B. Zou, B.-H. Liu, Y.-F. Huang, and G.-C. Guo, Phys. Rev. A **75**, 052310 (2007).
 - [3] A. Migdall, Physics Today **52**, 41 (1999).
 - [4] A. Fraine, O. Minaeva, D. S. Simon, R. Egorov, and A. V. Sergienko, Opt. Express **20**, 2025 (2012).
 - [5] N. Uribe-Patarroyo, A. Fraine, D. S. Simon, O. Minaeva, and A. V. Sergienko, Phys. Rev. Lett. **110**, 043601 (2013).
 - [6] N. Shenvi, J. Kempe, and K. B. Whaley, Phys. Rev. A **67**, 052307 (2003).
 - [7] J. Svozilfk, R. d. J. León-Montiel, and J. P. Torres, Phys. Rev. A **86**, 052327 (2012).
 - [8] D. Bouwmeester, J.-W. Pan, K. Mattle, M. Eibl, H. Weinfurter, and A. Zeilinger, Nature **390**, 575 (1997).
 - [9] G. Ribordy, J. Brendel, J. Gautier, N. Gisin, and H. Zbinden, Phys. Rev. A **63**, 012309 (2000).
 - [10] T. E. Chapuran, P. Toliver, N. A. Peters, J. Jackel, M. S. Goodman, R. J. Runser, S. R. McNown, N. Dallmann, R. J. Hughes, K. P. McCabe, et al., New J. Phys. **11**, 105001 (2009).
 - [11] H. C. Lim, A. Yoshizawa, H. Tsuchida, and K. Kikuchi, Opt. Express **26**, 22099 (2008).
 - [12] J. Svozilfk, M. Hendrych, A. S. Helmy, and J. P. Torres, Opt. Express **19**, 3115 (2011).
 - [13] W. H. Louisell, A. Yariv, and A. E. Siegman, Phys. Rev. **124**, 1646 (1961).
 - [14] D. Magde and H. Mahr, Phys. Rev. Lett. **18**, 905 (1967).
 - [15] S. E. Harris, M. K. Oshman, and R. L. Byer, Phys. Rev. Lett. **18**, 732 (1967).
 - [16] R. W. Boyd, *Nonlinear Optics* (Academic Press, 2008), 3rd ed.
 - [17] G. Brida, M. V. Chekhova, I. P. Degiovanni, M. Genovese, G. K. Kitaeva, A. Meda, and O. A. Shumilkina, Phys. Rev. Lett. **103**, 193602 (2009).
 - [18] J. Svozilfk and J. Peřina Jr., Phys. Rev. A **80**, 023819 (2009).
 - [19] A. Helmy, P. Abolghasem, J. Stewart Aitchison, B. Bijlani, J. Han, B. Holmes, D. Hutchings, U. Younis, and S. Wagner, Laser Photon. Rev. **5**, 272 (2011).
 - [20] A. S. Helmy, B. Bijlani, and P. Abolghasem, Opt. Lett. **32**, 2399 (2007).
 - [21] J. Peřina Jr., M. Centini, C. Sibilina, M. Bertolotti, and M. Scalora, Phys. Rev. A **73**, 033823 (2006).
 - [22] J. Peřina Jr., Phys. Rev. A **84**, 053840 (2011).
 - [23] M. M. Fejer, G. A. Magel, D. H. Jundt, and R. L. Byer, IEEE J. Quant. Electr. **28**, 2631 (1992).
 - [24] K. P. Huy, A. T. Nguyen, E. Brainis, M. Haelterman, P. Emplit, C. Corbari, A. Canagasabey, P. G. Kazansky, O. Deparis, A. A. Fotiadi, et al., Opt. Express **15**, 4419 (2007).
 - [25] J. Zhang, Master's thesis, Department of Electrical and Computer Engineering, University of Toronto (2008).
 - [26] A. Canagasabey, C. Corbari, F. Liegeois, A. Gladyshev, S. Guillemet, Y. Hernandez, E. Dianov, M. Ibsen, and P. Kazansky, in *Lasers and Electro-Optics 2009 and the*

- European Quantum Electronics Conference. CLEO Europe - EQEC 2009. European Conference on* (2009), p. 1.
- [27] T. G. Euser, G. Whyte, M. Scharrer, J. S. Y. Chen, A. Abdolvand, J. Nold, C. F. Kaminski, and P. S. J. Russell, *Opt. Express* **16**, 17972 (2008).
- [28] S. Ramachandran, P. Kristensen, and M. F. Yan, *Opt. Lett.* **34**, 2525 (2009).
- [29] N. Bozinovic, Y. Yue, Y. Ren, M. Tur, P. Kristensen, H. Huang, A. E. Willner, and S. Ramachandran, *Science* **340**, 1545 (2013).
- [30] Y. Yue, Y. Yan, N. Ahmed, J.-Y. Yang, L. Zhang, Y. Ren, H. Huang, K. M. Birnbaum, B. I. Erkmen, S. Dolinar, et al., *IEEE Phot. J.* **4** (2012).
- [31] A. Christ, K. Laiho, A. Eckstein, T. Lauckner, P. J. Mosley, and C. Silberhorn, *Phys. Rev. A* **80**, 033829 (2009).
- [32] H. Herrmann, X. Yang, A. Thomas, A. Poppe, W. Sohler, and C. Silberhorn, *Opt. Express* **21**, 27981 (2013).
- [33] G. Harder, V. Ansari, B. Brecht, T. Dirmeier, C. Marquardt, and C. Silberhorn, *Opt. Express* **21**, 13975 (2013).
- [34] M. Jachura, M. Karpinski, C. Radzewicz, and K. Banaszek, *Opt. Express* **22**, 8624 (2014).
- [35] E. Y. Zhu, Z. Tang, L. Qian, L. G. Helt, M. Liscidini, J. E. Sipe, C. Corbari, A. Canagasabay, M. Ibsen, and P. G. Kazansky, *Phys. Rev. Lett.* **108**, 213902 (2012).
- [36] M. Padgett and R. Bowman, *Nature Photonics* **5**, 343 (2011).
- [37] B. Guan, R. P. Scott, C. Qin, N. K. Fontaine, T. Su, C. Ferrari, M. Cappuzzo, F. Klemens, B. Keller, M. Earnshaw, et al., *Optics Express* **22**, 145 (2014).
- [38] C. S. Hamilton, A. Gábris, I. Jex, and S. M. Barnett, *New J. Phys.* **13**, 013015 (2011).
- [39] S. K. Goyal, F. S. Roux, A. Forbes, and T. Konrad, *Phys. Rev. Lett.* **110**, 263602 (2013).
- [40] L.-P. Deng, H. Wang, and K. Wang, *JOSA B* **24**, 2517 (2007).
- [41] C. T. Schmiegelow and F. Schmidt-Kaler, *Eur. Phys. J. D.* **66**, 1 (2012).
- [42] X. Li, P. L. Voss, J. E. Sharping, and P. Kumar, *Phys. Rev. Lett.* **94**, 053601 (2005).
- [43] J. Fulconis, O. Alibart, W. Wadsworth, P. Russell, and J. Rarity, *Opt. Express* **13**, 7572 (2005).
- [44] J. Fan, A. Migdall, and L. J. Wang, *Opt. Lett.* **30**, 3368 (2005).
- [45] L. Mandel and E. Wolf, *Optical Coherence and Quantum Optics* (Cambridge Univ. Press, Cambridge, 1995).
- [46] E. Y. Zhu, L. Qian, L. G. Helt, M. Liscidini, J. E. Sipe, C. Corbari, A. Canagasabay, M. Ibsen, and P. G. Kazansky, *Opt. Lett.* **35**, 1530 (2010).
- [47] C. Yeh and F. Shimabukuro, *The Essence of Dielectric Waveguides* (Springer, 2010).
- [48] W. Vogel, D. G. Welsch, and S. Walentowicz, *Quantum Optics* (Wiley-VCH, Weinheim, 2001).
- [49] B. Huttner, S. Serulnik, and Y. Ben-Aryeh, *Phys. Rev. A* **42**, 5594 (1990).
- [50] V. Brückner, *Elements of Optical Networking* (Springer Fachmedien Wiesbaden GmbH: Vieweg+Teubner Verlag, 2011).
- [51] T. L. Huynh, Tech. Rep., Dept. Electrical Computer Systems Engineering, Monash University (2004).
- [52] A. W. Snyder and J. D. Love, *Optical Waveguide Theory* (Chapman & Hall, London, 1983).
- [53] J. Peřina Jr., A. V. Sergienko, B. M. Jost, B. E. A. Saleh, and M. C. Teich, *Phys. Rev. A* **59**, 2359 (1999).
- [54] C. K. Law and J. H. Eberly, *Phys. Rev. Lett.* **92**, 127903 (2004).
- [55] G. Molina-Terriza, J. P. Torres, and L. Torner, *Phys. Rev. Lett.* **88**, 013601 (2001).
- [56] C. I. Osorio, G. Molina-Terriza, and J. P. Torres, *Phys. Rev. A* **77**, 015810 (2008).
- [57] J. T. Barreiro, N. K. Langford, N. A. Peters, and P. G. Kwiat, *Phys. Rev. Lett.* **95**, 260501 (2005).
- [58] D. Kang, L. G. Helt, S. V. Zhukovsky, J. P. Torres, J. E. Sipe, and A. S. Helmy, *Phys. Rev. A* **89**, 023833 (2014).
- [59] M. Karpinski, C. Radzewicz, and K. Banaszek, *Appl. Phys. Lett.* **94**, 181105 (2009).
- [60] R. Machulka, J. Svozilík, J. Soubusta, J. Peřina Jr., and O. Haderka, *Phys. Rev. A* **87**, 013836 (2013).
- [61] J. Svozilík and J. Peřina Jr., *Opt. Express* **18**, 27130 (2010).
- [62] S. Carrasco, J. P. Torres, L. Torner, A. V. Sergienko, B. E. A. Saleh, and M. C. Teich, *Opt. Lett.* **29**, 2429 (2004).
- [63] J. Svozilík, J. Peřina Jr., and J. P. Torres, *Phys. Rev. A* **86**, 052318 (2012).
- [64] M. Fokine, L. E. Nilsson, A. Claesson, D. Berlemont, L. Kjellberg, L. Krummenacher, and W. Margulis, *Opt. Lett.* **27**, 1643 (2002).
- [65] J. F. Clauser, M. A. Horne, A. Shimony, and R. A. Holt, *Phys. Rev. Lett.* **23**, 880 (1969).
- [66] R. Horodecki, P. Horodecki, and M. Horodecki, *Phys. Lett. A* **200**, 340 (1995).
- [67] M. McLaren, M. Agnew, J. Leach, F. S. Roux, M. J. Padgett, R. W. Boyd, and A. Forbes, *Opt. Express* **20**, 23589 (2012).
- [68] J. Leach, B. Jack, J. Romero, M. Ritsch-Martens, R. Boyd, A. Jha, S. Barnett, S. Franke-Arnold, and M. Padgett, *Opt. Express* **17**, 8287 (2009).